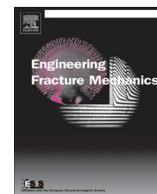




ELSEVIER

Contents lists available at ScienceDirect

## Engineering Fracture Mechanics

journal homepage: [www.elsevier.com/locate/engfracmech](http://www.elsevier.com/locate/engfracmech)

# Microscopic strain fields at crack tips in porous materials analyzed by a gradient-enhanced elasticity theory

T. Joffre, S. Chen, P. Isaksson\*

Solid Mechanics, The Ångström Laboratory, Uppsala University, Box 534, SE-751 21 Uppsala, Sweden

## ARTICLE INFO

## Article history:

Received 17 October 2015

Received in revised form 12 June 2016

Accepted 7 October 2016

Available online xxxx

## Keywords:

Porous materials

Fracture

Gradient enhanced elasticity

## ABSTRACT

The microstructural influence on the strain field at opening mode crack tips in porous materials, and especially its practical implication for understanding macroscopic failure, i.e. on a scale above, is investigated. Theoretical subscale microstrain fields are approximated using a gradient-enhanced elasticity theory and compared to microstrain fields computed in discrete high-resolution finite element microstructural models having varying pore densities but similar macroscopic geometry and boundary conditions as the theoretical gradient-enhanced model. The numerical elastic microstrain and microstress fields are non-singular in strong contrast to the singular macroscopic fields in classical linear elastic fracture theories. Experimentally approximated microstrain fields, estimated with a digital image correlation algorithm on images obtained in X-ray computational tomography fracture tests on a small wood specimen, are used to contrast the numerical analyses. A key observation is that an internal length parameter, used in the gradient-enhanced model, seems to be linked to the average pore diameter, allowing for direct bridging between scales.

© 2016 Published by Elsevier Ltd.

## 1. Introduction

How does a material's porous microstructure affect its macroscopic fracture behavior? Traditionally, deformation and fracture analysis of porous materials have been performed using classical continuum theories on the macroscale, cf. [1,4,5,25], omitting that these continuum theories were designed to describe deformation phenomena that could be captured by the naked eye. However, in materials where inherent heterogeneities such as pores, holes, embossings or cells are relatively large compared to the size of natural defects or cracks, global scale deformation fields given by classical continuum mechanics theories are distorted due to the complex deformations taking place at subscales, a phenomenon that is commonly referred to as length effects. Some well-known materials displaying such multiscale structural behavior are wood [1,2], impressed paper [3], solid foams [27] or embossed textiles.

Fig. 1 briefly visualizes the multiscale problem and illustrates the need to include subscale fields. Imagine a planar square domain of a material with small pores on the microscale. While on the macroscale, Fig. 1a, the material is considered continuous and homogeneous, the material is discontinuous and heterogeneous on the microscale, Fig. 1b. When the material becomes subject to a homogeneous and uniaxial load in the vertical direction, the resulting strain  $\varepsilon_{yy}$  is homogeneous on the macroscale and captures the value  $\varepsilon_0$ , Fig. 1c. On the microscale, Fig. 1d, the local microscopic strain fluctuates due to the

\* Corresponding author.

E-mail address: [per.isaksson@angstrom.uu.se](mailto:per.isaksson@angstrom.uu.se) (P. Isaksson).

### Nomenclature

$\rho$	relative density
$C_{ijkl}, C_{ijkl}^\mu$	material stiffness tensor (macro, micro)
$\sigma_{ij}, \sigma_{ij}^\mu, \bar{\sigma}_{ij}, \tilde{\sigma}_{ij}$	stress tensor (macro, micro, gradient enhanced, interpolated)
$\varepsilon_{ij}, \varepsilon_{ij}^\mu, \bar{\varepsilon}_{ij}, \tilde{\varepsilon}_{ij}$	strain tensor (macro, micro, gradient enhanced, interpolated)
$K_1$	macroscopic stress intensity factor
$c$	internal characteristic length
$l_c$	average cell diameter
$E, \nu$	macroscopic elastic constants (Young's modulus, Poisson's ratio)
$\bar{\varepsilon}_0, \bar{\sigma}_0$	microscopic maximum normal strain and cohesive stress

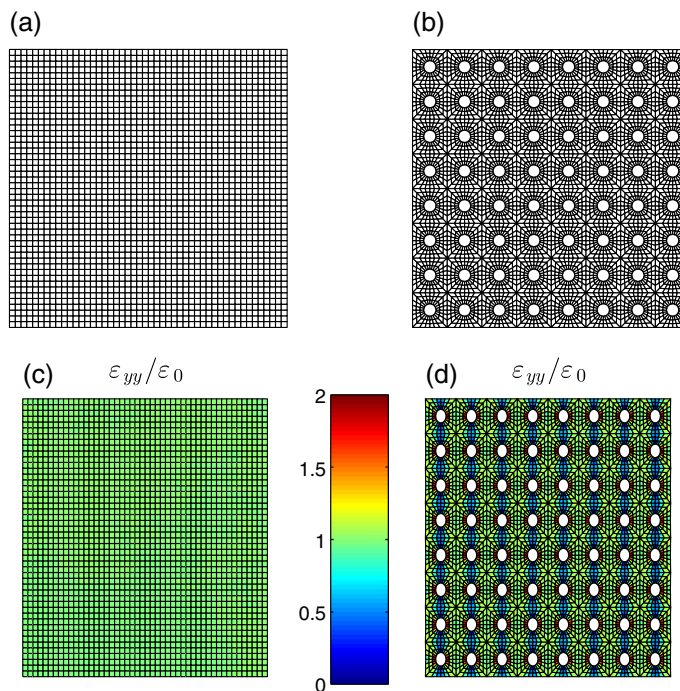


**Fig. 1.** (a) A material is considered homogeneous on the macroscale, but is heterogeneous and discontinuous on the microscale (b). (c) Homogeneous macrostrain field of magnitude  $\varepsilon_0$ , and non-homogeneous subscale microstrain field (d).

variations in the microstructure and can be twice as high at the vicinity of the pores. Linking the strain field on the subscale to the strain field on the scale above is mathematically difficult, especially if the subscale deformation is non-homogeneous and gradients are present, such as in the vicinity of crack tips, defects or pores (and even more so if the defects/pores are randomly positioned).

One realizes that the wide range of length scales affecting deformation and fracture in such kind of materials poses a difficult modeling problem, because the relation between the discontinuous microstructure and the prevailing deformation/fracture processes leads to inherent size effects. Thus, if one aims at a material description above the scale of a discrete discontinuous substructure, i.e. within a macroscopic continuum model, it is clear that any fracture model of such materials has to capture these length-scale effects occurring at subscales. Historically, the crack-tip problem has attracted much attention and many models have been suggested for different materials to eliminate unphysical stress and strain singularities appearing in classical theories of elasticity, which assume the material being idealized continuums, e.g. the early models of Barenblatt [6] and Dugdale [7]. To obtain general mathematical theories, much work has been done in the field of nonlocal and gradient elasticity, which includes length parameters in the models that limit the magnitude of stress and strain. The physical motivation to introduce gradient theories was originally presented in the early 1960s by Toupin [8] and Kröner

[9]. During that decade much work emerged in the field, e.g. Mindlin [10] and Kröner [11]. Since then, numerous nonlocal and gradient theories incorporating internal material length scales have been suggested, cf. the pioneering works by Eringen et al. [12,13] or Aifantis et al. [14–18]. Later work includes [19,20]. The simplicity and attraction of the pioneer Aifantis and co-workers' formulations relies in that only one additional constitutive parameter is required. However, the proposed solutions have resulted in some controversy, mainly because the derived stress fields may not be divergence-free, or satisfy the compatibility equations, according to classical theories of continuum mechanics. Some details and physical explanations are still lacking, but the gradient enhanced theory has been observed to capture experimental behavior of heterogeneous materials fairly well, cf. [21], although not perfect. As pointed out by Aifantis [18], there is still no available framework for relating internal material lengths to physical properties even though the need has been documented in several studies, e.g. [21–24]. The lengths are usually treated as pure phenomenological fitted constants and not much progress has been made toward their physical identification through microstructure simulations or laboratory tests.

This study aims at examine such length-scale effects in deformation fields in porous materials by analyzing -theoretically and numerically- strain fields at in-plane mode I crack tips on macro- and microscales. To compare the numerically approximated strain fields with an estimated “real” strain field in a porous material on the microscopic scale, X-ray computational tomography fracture experiments are performed on a wood specimen and subsequently analyzed with digital image correlation techniques.

## 2. Experimental observation

A crack in the  $TR$ -plane in wood, i.e. a crack that extend in the radial direction with its crack lips perpendicular to the tangential direction (Fig. 2a), is considered to visualize the phenomenon. Thuvander and Berglund [4] studied such fractures and reported that the crack advances in a step-wise fashion by separating cell walls in the middle lamella (Fig. 2b). At slowly increased mechanical loading, a radial crack advance one cell diameter and then arrest until the global load is increased sufficiently enough to drive the crack further [4]. Stanzl-Tschegg et al. [5] report that a change in wall thickness or cell size terminates crack growth. Previous studies thus indicate that a prevailing fracture mechanism in wood is controlled by its microstructural properties.

X-ray computed tomography (CT) is a non-destructive technique to measure material density throughout a volume. The equipment used, a SkyScan-1172, has a resolution high enough to distinguish individual cells in wood. The instrument has a built-in tensile stage, which was used to load a small specimen (made of Norway spruce) of size  $5 \times 5 \times 4$  mm containing a natural flaw. The natural flaw, about 2 mm long, was oriented along the radial direction with its crack lips perpendicular to the tangential direction. The cracked specimen was mounted on a slowly rotating holder that allows X-rays to enter from different directions. Two-dimensional projection images were then taken in a multitude of directions, which allows subsequent reconstruction of the 3D microstructure. The specimen was loaded stepwise in-situ by displacements given to its horizontal boundaries. At some steps, see Fig. 3, CT scans were performed allowing for successive images showing the evolving deformation process. During each scan, 1600 radiographs were taken over 180 degrees with a pixel size of  $2 \mu\text{m}$ . The average diameter of the cells is about  $20 \mu\text{m}$ . It should be noticed that the crack is growing in earlywood, i.e. no transition between earlywood and latewood is considered in this study.

Two-dimensional deformation fields of the wood's internal structure were estimated by a digital image correlation algorithm [26] using cross-section images at consecutive load steps. In connection to this it is worth mention that while for most materials a random pattern must be applied to the surface of the specimen that deforms along with the object when doing image correlation analyses, for wood there is no need for this due to the inherent irregular pattern of the porous microstructure.

The near straight line that denotes the force-displacement response in Fig. 3 indicates that irreversible deformations is small, i.e. plasticity is limited, meaning that an assumption that the material remains in its linearly elastic regime through the loading process is feasible. However, some (small) mechanical relaxation may be noticed.

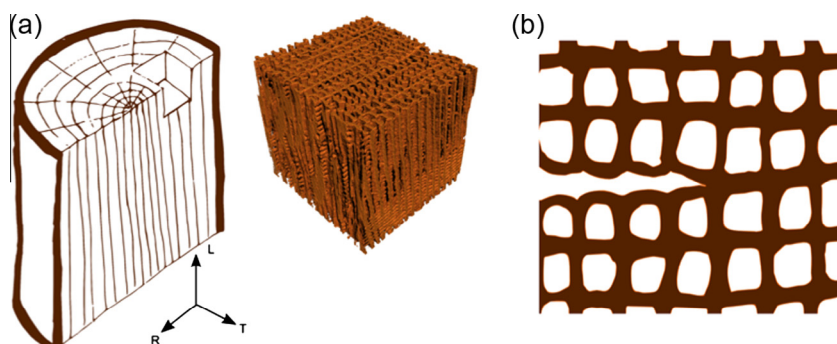


Fig. 2. (a) Illustration of the porous structure of wood (b) A crack advances in-between the pores (cells), in the lamella, in the  $TR$ -plane.

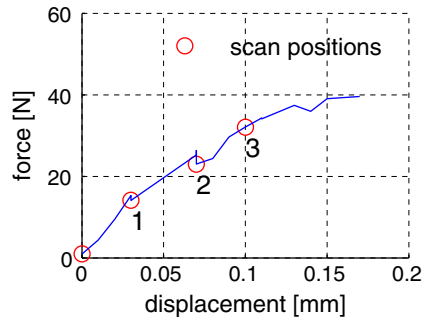


Fig. 3. Load-displacement curve in the CT experiment.

The deformation of a  $400 \times 400 \mu\text{m}$  domain surrounding the crack tip was used for the calculations. A correlation algorithm divides the image taken at a load step in a number of overlapping subset images, which are tracked in the image taken in the successive load step. In the correlation procedure, a displacement field is numerically approximated and refined to obtain a continuous field [26]. The average pore diameter is about 10 pixels, which poses a significant limitation on the subset size, since the latter must contain enough distinct features to yield a good correlation. A too small subset size tends to be affected by the noise present in each image while a too large subset size smoothen the field to such extent that the deformation field is not correctly captured. Thus, the image correlation analysis involves a trade-off between spatial resolution and resolving small-scale displacements and strains. In our case, the subsets need to be fairly larger than the representative irregular pattern constituted by some few pores, wherefore a subset radius of 20 pixels was used. The strain field is finally estimated by spatial differentiation of the approximated displacement field.

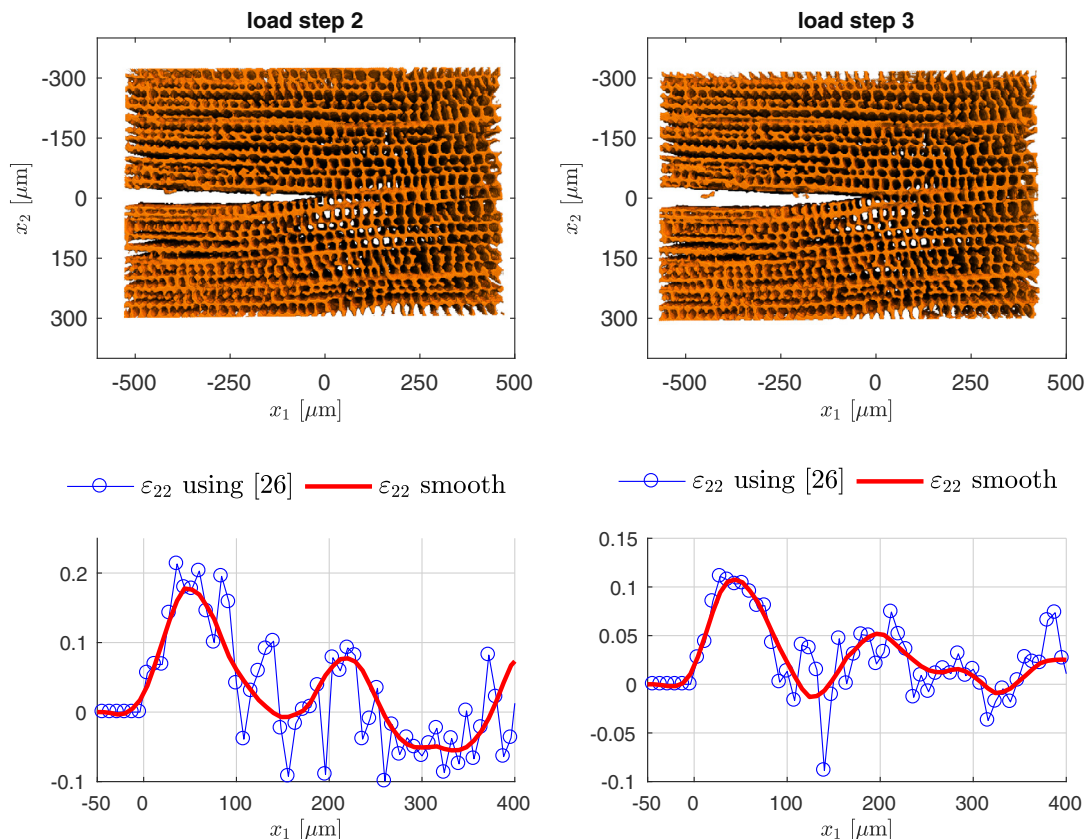


Fig. 4. Upper row: Parts of reconstructed images of the fracturing wood in the radial plane. Note the natural crack, extending from the left in two scan steps 2–3 indicated in Fig. 3. Lower row: estimated strain fields  $\varepsilon_{22}$  along the crack plane, evaluated from the images obtained in scans 2–3 using the digital image correlation algorithm [26]. To magnify perceptibility, a smoothed strain (using the robust “loess” Matlab function) is also displayed. The tip is always positioned at  $x_1 = 0$ , i.e. the origin moves when the crack grows. The strains have manually been put to zero at  $x_2 = 0$  and  $x_1 < 0$ .

Fig. 4 shows the normal strain  $\varepsilon_{22}$  estimated in the CT experiments at two different crack lengths and load steps along the crack plane ahead of the tip (the  $x_2$ -direction is perpendicular to the crack plane). The tip is always located at the origin in the graphs.

It is underlined that analyzing these types of experiments is far from easy. The material is complex and discontinuous with large cells and the strains fluctuate heavily. The resolution of the CT images (pixel size  $2\ \mu\text{m}$ ), together with the need to define sufficiently large subset images for the correlation algorithm (circular domains of radius 20 pixels), produces deformation and strain fields that are not accurately enough for a complete description of the cell wall deformations. The reason for having relatively large subsets, in comparison to the pore size, is because the correlation algorithm needs sufficiently large domains to be able to track the reference pattern. Furthermore, strains are even more difficult to accurately estimate than displacements, because differentiation is sensitive to noise. This means that any noise and error in the displacement field will magnify errors in the calculated strain fields. Additionally, it is very difficult –perhaps impossible– to determine the exact position of the physical crack tip. All these limitations and error sources should be kept in mind while evaluating the experimentally estimated strain fields. Some trends may nevertheless be imagined. The estimated fields indicates that the position of maximum strain is located at some distance ahead of the crack tip, a distance that seems to be of the same order of magnitude as the average pore diameter. There is incertitude about the exact value estimated at the crack tip due to the discontinuity in displacements and the limitations in resolution and image correlation. However, the tendency of an increase in normal strain ahead of the crack can most likely not be explained only by these circumstances and is thus pointing toward the presence of peak strain ahead of the tip. The experiments seem to confirm the conclusions in [4,5]. However, we need to obtain higher resolved CT images and also many more experiments to be convinced and be able to draw stronger and trustworthy conclusions.

### 3. Theory

The porous material is considered transversely isotropic and linearly elastic on the macroscopic scale and a state of plane strain prevails. Small strains are assumed. An important parameter of porous materials is the relative density  $\rho$  ( $0 \leq \rho \leq 1$ ), given by the ratio of volume of the solid material in relation to the pore space. Gibson and Ashby [27] reports that for a transversely isotropic *open* porous material, the relation between the material stiffness tensor  $C_{ijkl}^\mu$  on the microscale and the material stiffness tensor  $C_{ijkl}$  on the macroscale can be fairly well approximated by

$$C_{ijkl} = \rho^2 C_{ijkl}^\mu. \quad (1)$$

It is further assumed that the *average* strain and stress fields on the microscale are continuous even though the discrete microstructure is discontinuous. Let the average stress tensor on the microscale be denoted  $\sigma_{ij}^\mu$  and let its counterpart on the macroscale be denoted  $\sigma_{ij}$ . The microscopic elastic strain tensor  $\varepsilon_{ij}^\mu$  is given by Hooke's generalized law  $\varepsilon_{ij}^\mu = [\sigma_{ij}^\mu(1 + \nu) - \nu\sigma_{kk}^\mu\delta_{ij}]/E^\mu$ , where  $E^\mu$  is Young's modulus on the microscale and  $\delta_{ij}$  is Kronecker's delta. Similarly, on the macroscopic scale,  $E$  is Young's modulus and the macroscopic elastic strain tensor  $\varepsilon_{ij}$  is given by  $\varepsilon_{ij} = [\sigma_{ij}/(1 + \nu) - \nu\sigma_{kk}\delta_{ij}]/E$ . The Poisson's ratio  $\nu$  is assumed to be equal on the two scales. An assumption of elastic strain energy equivalence is made, which means that the elastic strain energy density in a material element is equal on the microscopic and macroscopic scales, i.e. at an arbitrary material point  $\sigma_{ij}^\mu\varepsilon_{ij}^\mu = \sigma_{ij}\varepsilon_{ij}$ . Then, using (1), the following relations hold:

$$\varepsilon_{ij}^\mu = \rho\varepsilon_{ij} \text{ and } \sigma_{ij}^\mu = \rho^{-1}\sigma_{ij}. \quad (2)$$

Consider a macroscopic body containing a straight stationary crack, illustrated in Fig. 5.

A Cartesian  $(x_1, x_2)$  and a polar coordinate system  $(r = [x_1^2 + x_2^2]^{1/2}, \theta = \tan^{-1}[x_2/x_1])$  are introduced with their origins coinciding with the crack-tip. The crack occupies the negative part of the  $x_1$ -axis, i.e.  $x_1 < 0$  and  $x_2 = 0$ . The extent of the body in the  $x_3$ -direction is large and a state of plane strain prevails. Distant from the crack-tip a pure mode I opening field acts and the singular macroscopic stress tensor  $\sigma_{ij}$  is given by:

$$\sigma_{ij} = K_I[2\pi r]^{-1/2}f_{ij}(\theta) \text{ as } r \rightarrow \infty, \quad i, j = 1, 2. \quad (3)$$

where  $K_I$  is the LFM mode I stress intensity factor, cf. Williams [28]. The macroscopic displacement field  $u_i$  producing the stress field in (3) is given by

$$u_i = (1 + \nu)K_I[r/(8\pi)]^{1/2}g_i(\theta)/E \text{ as } r \rightarrow \infty. \quad (4)$$

The angular functions  $f_{ij}(\theta)$  and  $g_i(\theta)$  in (3) and (4) are found in every book on fracture mechanics.

Several techniques have over the years been suggested to extend traditional continuum formulations to include gradient sensitivity. A convenient approach, cf. [29], is to compute a nonlocal microscopic stress tensor  $\bar{\sigma}_{ij}$ , in a point  $(x_1, x_2)$ , as the weighted average of the local microscopic stresses  $\sigma_{ij}^\mu$  in a surrounding domain  $\Omega$ ,

$$\bar{\sigma}_{ij}(x_1, x_2) = \Psi^{-1} \int_{\Omega} \phi(\zeta)\sigma_{ij}^\mu(x'_1, x'_2)d\Omega(x'_1, x'_2), \quad \Psi = \int_{\Omega} \phi(\zeta)d\Omega, \quad (5)$$

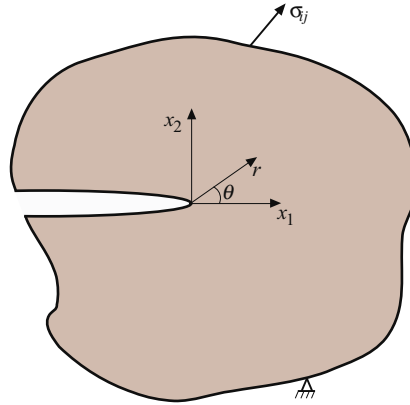


Fig. 5. Load and geometry on macroscopic scale.

where  $\zeta$  is the distance between  $(x_1, x_2)$  and  $(x'_1, x'_2)$ ,  $\phi$  a symmetric interaction kernel and  $\Psi$  a scaling factor that secure that the two stress tensors are equal for a homogenous stress state in  $\Omega$ . The nonlocal formulation (5) is based on an assumption of mechanical interactions on the microscale (e.g. via connected cell walls) and can for sufficiently smooth fields of  $\sigma_{ij}^{\mu}$  be rewritten into a gradient formulation around  $(x_1, x_2)$  according to a Taylor expansion, cf. [16,30],

$$\sigma_{ij}^{\mu}(x'_1, x'_2) = \sum_{k=0}^n \sum_{l=0}^n \frac{(x'_1 - x_1)^k (x'_2 - x_2)^l}{k!l!} \frac{\partial^k \partial^l \sigma_{ij}^{\mu}(x_1, x_2)}{\partial x_1^k \partial x_2^l}, \tag{6}$$

where  $n$  denote the order of the series expansion. Dropping unsymmetrical terms in (6), yields after substitution of (6) into (5),

$$\bar{\sigma}_{ij}(x_1, x_2) = \sigma_{ij}^{\mu}(x_1, x_2) + \frac{1}{m!} c^{2m} \nabla^{2m} \sigma_{ij}^{\mu}(x_1, x_2) + \dots \quad m = 1, 2, \dots \tag{7}$$

where the range of microscopic nonlocal actions is given by an *internal microstructural length*  $c$  through a symmetric interaction kernel  $\phi = \exp[-\zeta^2 / (4c^2)] / [4\pi c^2]$ . For simplicity, the gradient enhancement is here considered isotropic, despite the fact that many porous materials may be strongly anisotropic (e.g. wood, bone or paper). Here, we aim to illustrate the complex mechanical phenomenon rather than derive a general theory. However, it is possible to extend the formulation (7) to include anisotropic gradient-sensitive lengths, cf. Gitman et al. [45].

Now, taking the Laplacian of (7), subtract from the original (7), and neglect derivatives of the forth order and higher, an implicit gradient formulation is obtained in the form of a modified inhomogeneous Helmholtz equation, cf. [16,29],

$$\bar{\sigma}_{ij} - c^2 \nabla^2 \bar{\sigma}_{ij} = \sigma_{ij}^{\mu}, \tag{8}$$

where the dependence of the coordinates has been dropped. Now, using (2), a mode I gradient-enhanced stress tensor on the subscale can be approximated using the macroscopic LEFM stress tensors (3) as source terms in (8), i.e.,

$$\bar{\sigma}_{ij} - c^2 \nabla^2 \bar{\sigma}_{ij} = \rho^{-1} K_1 [2\pi r]^{-1/2} f_{ij}(\theta). \tag{9}$$

As seen in (9), in the limit  $c \rightarrow 0$  and  $\rho \rightarrow 1$  the classical macroscopic LEFM fields in (3) are recovered. In addition to physical conditions of traction-free crack surfaces, requirement of finite stresses when  $r \rightarrow 0$ , and  $\bar{\sigma}_{ij} \rightarrow \sigma_{ij}$  when  $r/c \rightarrow \infty$  and  $\rho \rightarrow 1$  leads to the following expressions of the normal stress components of the gradient-enhanced subscale microstress when solving (9):

$$\begin{aligned} \bar{\sigma}_{11} &= \frac{K_1}{\rho\sqrt{2\pi r}} \left[ \frac{3}{4} \cos \frac{\theta}{2} [1 - e^{-r/c}] + \frac{1}{4} \cos \frac{5\theta}{2} [1 - 6c^2/r^2 + 2e^{-r/c}(3c^2/r^2 + 3c/r + 1)] \right] \\ \bar{\sigma}_{22} &= \frac{K_1}{\rho\sqrt{2\pi r}} \left[ \frac{5}{4} \cos \frac{\theta}{2} [1 - e^{-r/c}] - \frac{1}{4} \cos \frac{5\theta}{2} [1 - 6c^2/r^2 + 2e^{-r/c}(3c^2/r^2 + 3c/r + 1)] \right] \\ \bar{\sigma}_{33} &= \frac{K_1}{\rho\sqrt{2\pi r}} \left[ 2\nu \cos \frac{\theta}{2} [1 - e^{-r/c}] \right] \end{aligned} \tag{10}$$

A deeper discussion of gradient theories and the physical arguments leading to them is found in e.g. [17,18,31–33,39]. It is underlined that the gradient-enhanced stress  $\bar{\sigma}_{ij}$  should not be considered as a standard macrostress field but rather as a nonstandard subscale microstress field. When carefully examine (9) and (10), one may observe that in general  $\bar{\sigma}_{j,i} \neq 0$  wherefore the gradient-enhanced subscale microstress field is not divergence-free, nor does the gradient-enhanced strain fields

satisfy the classical compatibility equations in continuum mechanics. For discontinuous materials with holes, or pores, the classical compatibility equations may not be sufficient to guarantee that the strains can be obtained from single-valued displacement fields. It should be said that the physical meaning of having divergence in the gradient-enhanced stress field (and hence not traditional stress equilibrium) is not entirely understood and has lent some criticism. The theory may thus be questioned, and the interested reader is advised to e.g. [39] for a thorough discussion on this matter.

The equilibrium equation for the gradient-enhanced subscale stress  $\bar{\sigma}_{ij}$  may take the form  $\bar{\sigma}_{jij} = f_j$  where  $f_j$  is a gradient-sensitive internal body force taking into account subscale bulk-surface interaction, cf. [18,39], at internal pores, etc. The gradient-enhanced stress field may thus be interpreted so that it reflects the subscale stresses emerging from displacement jumps on a discontinuous subscale. Even though the meaning of  $\bar{\sigma}_{jij} \neq 0$  is still an open scientific question, the concept has proven powerful and the analytic solutions, e.g. [18], includes length scales and seemingly captures the subscale's discontinuous heterogenic structure. However, the theory obviously needs further investigations and deeper physical understanding to be more convincing and trustworthy. Nevertheless, we believe the strategy may help engineers to analyze fracture phenomena since length effects can be incorporated in the models fairly easy and thus reveal their importance. In connection to this it is worth mentioning that a substantial amount of studies during the last decades, cf. [40–44], have identified the need to include size-dependent strengthening/hardening associated with plastic deformations involving strain gradients and some different theories have been proposed. The suggested theories are fairly different with respect to the structure of the equations, however, each aims to capture boundary layer phenomena related to phase and grain boundaries, or slips in single crystals, within small deformation formulations. It is nowadays generally accepted that plasticity theories must be higher order, not only by incorporation strain gradients but also in having higher order stresses that are work conjugate to the strain gradients, cf. Hutchinson [40]. Furthermore, we remind that the macrostresses  $\sigma_{ij}$  and the macrostrains  $\varepsilon_{ij}$  are still given by the classical singular LEFM solutions, and the gradient-enhanced subscale microscopic elastic strain tensors  $\bar{\varepsilon}_{ij}$  are related to  $\bar{\sigma}_{ij}$  via Hooke's generalized law  $\bar{\varepsilon}_{ij} = [\bar{\sigma}_{ij}(1 + \nu) - \nu \bar{\sigma}_{kk} \delta_{ij}] / E^\mu$ . Hence, the strain field  $\bar{\varepsilon}_{ij}$  approximates the physical material behavior on the microscale in regions with high magnitudes of stress and strain gradients, cf. [17,21,34]. Applying the micro/macro stiffness approximation in (1), the subscale microstrain in the direction perpendicular to the crack plane is

$$\bar{\varepsilon}_{22} = \frac{\rho K_I (1 + \nu)}{E \sqrt{2\pi r}} \left[ \frac{5 - 8\nu}{4} \cos \frac{\theta}{2} [1 - e^{-r/c}] - \frac{1}{4} \cos \frac{5\theta}{2} [1 - 6c^2/r^2 + 2e^{-r/c}(3c^2/r^2 + 3c/r + 1)] \right] \quad (11)$$

Using a value of  $\nu = 0.3$ , (11) give that the maximum  $\bar{\varepsilon}_{22}$  is equal to  $0.2\rho K_I / [Ec^{1/2}]$  and located on the crack plane at  $r/c \approx 1$ .

In Fig. 6, the bounded subscale microscopic average strain distribution according to (11) ahead of the tip is shown, together with the microscopic singular LEFM-strain. The two strains are similar for  $r/c > 6$ .

#### 4. Finite element discrete microstructural model

The applicability of the gradient-enhanced theory to approximate subscale length effects on the macroscale is in the following judged by comparing the theory with discrete finite element microstructural models having identical macroscopic geometry and boundary conditions as the gradient-enhanced theory, but different discrete microstructural lengths (i.e. pore sizes and densities). The bodies are limited to circular discs with radius  $R$  and unit thickness with their centers located at the crack-tip, whereupon boundary layer problems are formulated.

The microstructural models are solved using well-established finite element algorithms implemented in a Matlab [35] code, discretized with 3-node isoparametric elements. Voronoi tessellation combined with the Distmesh algorithm [36] is employed for mesh generation. Planar meshes that contain randomly positioned and randomly shaped round pores of similar sizes are generated, which resembles porous cracked microstructures, Fig. 7.

In planar structures with evenly distributed round shaped pores (i.e. macroscopic isotropic bodies) the average pore diameter  $l_c$  can be approximated to [27]

$$l_c = 2[(1 - \rho)/\pi]^{1/2} / N_c, \quad (12)$$

where  $N_c$  is the average number of pores per unit length along a line in any direction. All structural meshes have  $N_c = 25$  and the cell walls are assumed isotropic with a Poisson's ratio equal to  $\nu = 0.3$ . Fig. 8 shows some examples of loaded structures with three different densities. The densest meshes contain about  $220 \cdot 10^3$  elements.

The aim is to compare the gradient-enhanced approximations of the subscale microstrains with those obtained in discrete structural finite element models of porous materials having different densities  $\rho$  and average pore diameters  $l_c$ . However, rather than using one solution for a unique configuration with a certain average pore diameter and density, *characteristic solutions* are used that consists of the union of solutions from 100 unique configurations having the same average pore diameter  $l_c$  and density  $\rho$  but different random seeds used for the mesh generation. A statistical variation is thus included in the analysis.

While the theoretical macroscopic normal strain fields are symmetric with respect to the  $x_1$ -axis, the scattered microstrain fields in the finite element solutions are not, because of the random unsymmetric porous microstructures. To circumvent this, the discrete microstrain fields are mirrored around their macroscopic symmetry axes, meaning that every unique integration point in the elements provide duplicate strains and positions: one at the integration point itself, at  $(x_1, x_2)$ , and

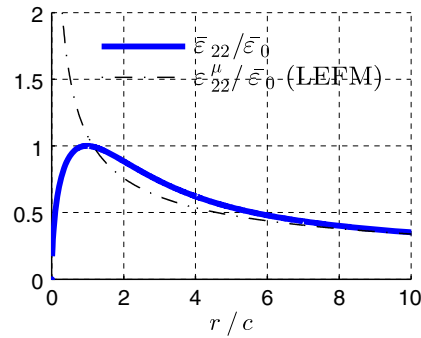


**Fig. 6.** Microscopic strain for  $\nu = 0.3$ ,  $\theta = 0$  and  $r/c \geq 0$  given by (11), contrasted with the classical singular LEFM solution. The gradient-enhanced strain  $\bar{\epsilon}_{22}$  is bounded and has its maximum located close to, but not exactly at, the tip, at  $r \approx c$ . The strains are normalized with  $\bar{\epsilon}_0 = 0.2\rho K_I/[Ec^{1/2}]$ .

another at the mirrored position  $(x_1, -x_2)$ . The union of 100 scattered strain fields is then interpolated on a quadratic grid covering the whole problem domain. The number of equally-sized square cells in the interpolating grid is determined so that, in average, each pore in the microstructure is covered by 50 squared grid-cells, as illustrated in Fig. 9a.

Since the structural meshes are circular, and not quadratic, about 20% of the grid cells are excluded in the interpolating scheme since they are located outside the meshes. This means that, depending on the mesh resolution, about 2–18 data points from each unique and mirrored porous mesh are located inside each interpolating grid cell, as illustrated in Fig. 9. Thus, about 200–1800 data points are in each grid-cell. Bicubic interpolation is applied to account for nonlinearities in the strain field. It is straightforward and follows established routines included in the Matlab code. However, the interpolation produces slightly discontinuous, or fluctuating, strain fields  $\epsilon_{ij}^\#$  on the scale above (i.e., the macroscopic scale), because of the scattered data, wherefore a smoothing algorithm is applied, Garcia [37,38]. This is a physical requirement since the interpolated strain fields should represent smooth continuous homogeneous fields in order to be compared to a theoretical subscale gradient-enhanced strain field  $\bar{\epsilon}_{ij}$ . The robust least-square based algorithm smooths the (slightly) discontinuous interpolated strain  $\epsilon_{ij}^\#$  using a cosine transform. The algorithm minimizes the influence of outlying data and determines the amount of smoothing carried out by a generalized cross-validation (GCV) method while securing physical boundary conditions prevails, i.e.  $\bar{\epsilon}_{11} = \bar{\epsilon}_{22} = \bar{\epsilon}_{12} = 0$  along the crack surfaces. The applied algorithm, `smoothn.m`, is available at the Matlab central file exchange server. The interested reader is advised to [37] and [38] for further details.

The interpolated slightly smoothed strain fields  $\bar{\epsilon}_{ij}$  should be interpreted as microscopic strains in equivalent homogeneous continuums representing typical subscale average strain fields in porous materials with a specific average pore diameter  $l_c$ , density  $\rho$ , and subject to a remote macroscopic mode I load. It is underlined that the equivalent microstrains represent the subscale microstrain fields *in an average sense*.

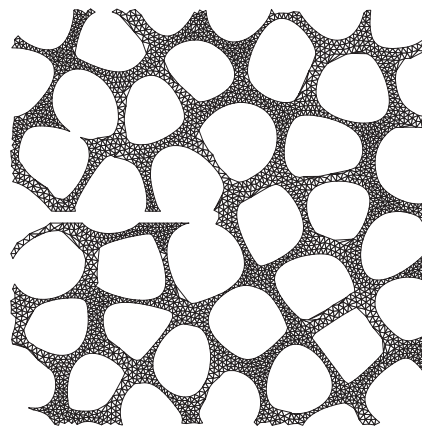


**Fig. 7.** Close-up of a crack-tip region in a typical microstructural mesh ( $\rho = 0.3$ ). The tip is located at the center of the figure and the straight crack extends to the left. The bodies are loaded so that a pure macroscopic mode I field is acting distant from the crack-tips. Boundary conditions are given as prescribed displacements given by (4).

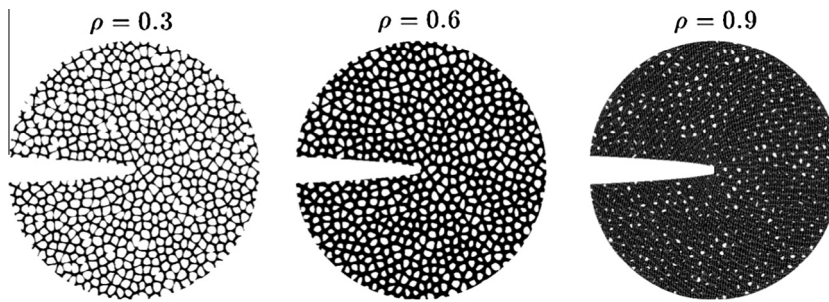


**Fig. 8.** Deformed (exaggerated) porous 2D meshes. The bodies are loaded in macroscopic mode I via displacements on their boundaries at  $r = R$ . In the limit  $\rho \rightarrow 1$ , the material approaches a continuum.

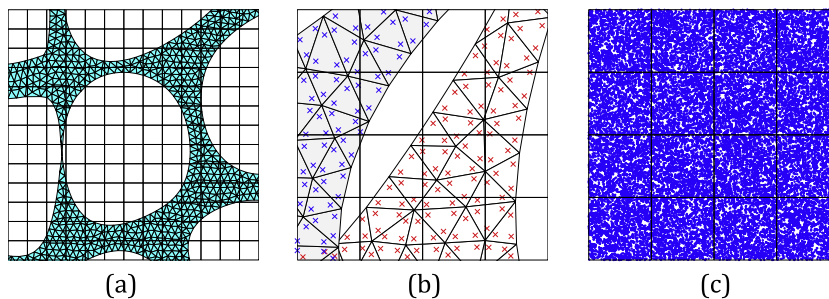


**Fig. 9.** (a) In average is each pore covered by 50 squared grid-cells. (b) Small part of one unique and mirrored porous mesh with integration points indicated. A part of the interpolation grid and the (triangular) elements' edges are also drawn. (c) Union of 100 unique mirrored structures attached to the same grid-part as in (b), forming a characteristic structure (only the data points are shown) reflecting an equivalent homogeneous continuum.

## 5. Results and discussion

### 5.1. Microstrains

It seems fair to assume that the porous material's characteristic length is controlled by the average pore diameter  $l_c$ . This assumption is somewhat in agreement with the experimental observations in [4,5] and the tendencies in Fig. 4. Fig. 10 shows the interpolated strain  $\tilde{\epsilon}_{22}$  computed from the union of solutions of 100 unique structural geometries in each set-up. The strain  $\tilde{\epsilon}_{22}$  reflects a typical porous material having certain inherent properties  $\rho$  and  $l_c$ . One may notice, in Fig. 10, that the maximum microstrain along the crack plane is relatively larger in magnitude and located closer to the tip in porous structures of higher densities compared to in those of lower densities. It is stressed that the different porous bodies are always loaded on their boundaries (with constant radii) with equal displacements given by (4). The length  $[K_1/E]^2$  is equal in all investigated cases.

Assuming that the characteristic length is controlled by the average pore diameter  $l_c$ , the theoretical maximum microstrain  $\bar{\epsilon}_{22}$  along the crack plane is given by  $\bar{\epsilon}_0 \approx 0.2\rho K_1/[El_c^{1/2}]$  and is located at one pore diameter ahead of the tip. In Fig. 11, the microstrains  $\tilde{\epsilon}_{22}$  are contrasted with the theoretical gradient-enhanced subscale microstrain  $\bar{\epsilon}_{22}$  given by (11), using  $l_c$  as the material characteristic length  $c$ .

As seen in Fig. 11, the overall mechanical behavior is fairly well captured even though it is not a perfect match. To reveal this observation further, Fig. 12 shows the distance  $x_0/l_c$  to the peak  $\tilde{\epsilon}_{22}$  along the crack plane, and also  $\max\{\tilde{\epsilon}_{22}\}$  compared to the theoretical counterpart  $\bar{\epsilon}_0$  at different densities  $\rho$  and average pore diameters  $l_c$ . Contours of normalized strains are shown in Fig. 13 for the special cases  $\rho = 0.4$  and  $\rho = 0.6$  to expose the near-tip fields.

As indicated in Figs. 12 and 13, the gradient-enhanced theory approximates both the position and magnitude of the subscale microstrain field  $\tilde{\epsilon}_{22}$  fairly well. For relative densities less than  $\approx 0.7$  the ratio  $x_0/l_c \rightarrow 1$ , while for higher densities the ratio  $x_0/l_c$  is a bit larger but still less than 4. This is not surprising. When  $\rho \rightarrow 1$ , the porous material approaches a classical homogeneous elastic continuum whereupon the strains tend to infinity when  $x_1 \rightarrow 0$  while any characteristic length in the material vanishes. For high densities, the pores are small and the distances between them fairly large meaning that the material contains spread voids rather than connected pores. The observation that the characteristic length  $c$  is linked to the average pore size  $l_c$  is similar to earlier findings, cf. [46]. The result also supports other studies. In [21], it is reported that the average distance between adjacent connections in planar fiber-based materials gives an internal length scale parameter.

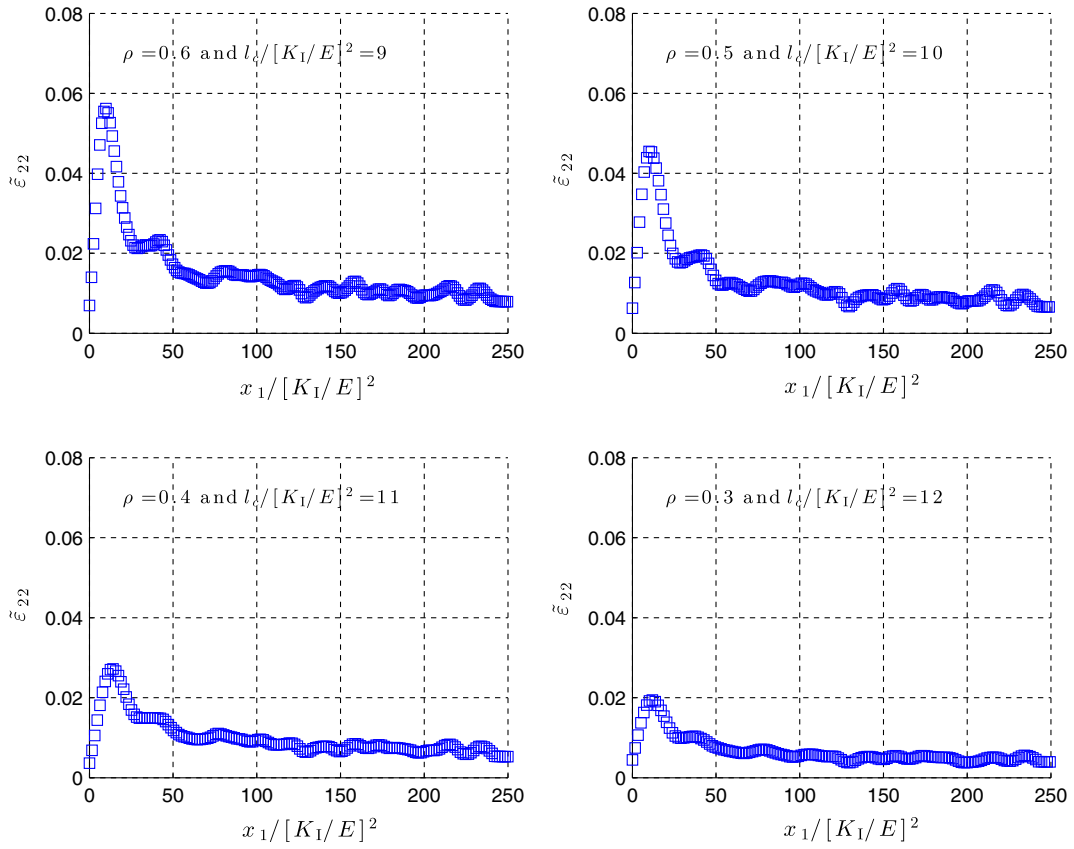


**Fig. 10.** Microstrain  $\bar{\varepsilon}_{22}$  ahead of the tip in characteristic structures of different density  $\rho$  and average pore diameter  $l_c$ . The spatial position  $x_1$  is normalized with the length  $[K_I/E]^2$ , which is equal in all cases.

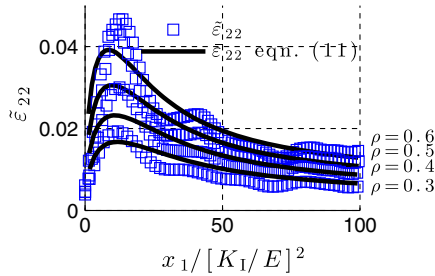


**Fig. 11.** Microstrains  $\bar{\varepsilon}_{22}$  contrasted with the gradient-enhanced subscale microstrain  $\bar{\varepsilon}_{22}$  given by (11) using  $c = l_c$ .

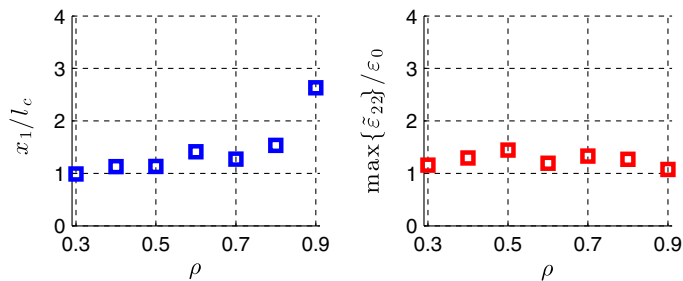


**Fig. 12.** (a) The location  $x_1 = x_0$  of maximum  $\bar{\varepsilon}_{22}$  along the crack plane, normalized with the average pore diameter  $l_c$ . (b) Magnitude of maximum microstrain  $\bar{\varepsilon}_{22}$  normalized with the theoretical  $\bar{\varepsilon}_0 = 0.2\rho K_I/[E l_c^{1/2}]$ .

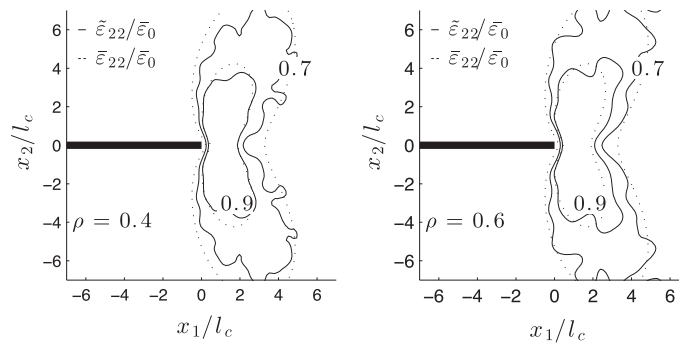


Fig. 13. Contours of microstrains  $\bar{\epsilon}_{22}/\bar{\epsilon}_0$  at densities  $\rho = 0.4$  and  $\rho = 0.6$ .

In [47], where fracture experiments on crystalline ceramics and metals are scrutinized, it is reported that the characteristic length can be directly linked to the average grain size.

A conclusion one may draw from the findings here is that the gradient-enhanced theory seems to capture the strain field on both the macroscopic scale and the microscopic subscale (i.e. Eqs. (2), (3), (10) and (11)) in transversely isotropic porous materials. The tendency observed from the image correlation analysis of the CT experiments, Fig. 4, seems to imply that the microstrain field at a fairly straight crack in a porous material is different compared to what is anticipated from classical continuum elasticity theory. The theoretical observation that the subscale microstrain field has its maximum at some pore diameter from the physical crack tip illustrates the difficulty to interpret the experiments. The average pore diameter in the examined wood material is about 20  $\mu\text{m}$ . Since it is very difficult (if possibly at all) to determine the exact position of the physical crack tip in the experiments together with the limitations in the image correlation analysis, we cannot tell for sure but rather imagine a tendency of peak strains ahead of the tip.

### 5.2. Note on incompatibility

The normal microstrain in the near-tip region is bounded (Fig. 12) for all analyzed densities  $\rho < 1$ . A key observation in Figs. 10–13 is that the microstrains in the microstructural models are finite in contrast to the classical singular LEFM strain field, which implies that the porous microstructure affects the mechanical behavior, meaning that traditional continuum theories are perhaps not accurate enough when analyzing fracture in porous materials because their lack of length scales. The gradient-enhanced model, on the other hand, seems to offer a fair approximation (however not exact) of the expected near-tip microstrain field despite the physical peculiarity of divergence in the gradient-enhanced subscale microstress field, as discussed in connection to (10), or incompatibility in the subscale microstrain field. However, for materials with pores the classical compatibility equations may not be sufficient to guarantee that the strains can be obtained from single-valued displacement fields. It is underlined, again, that the approximated gradient-enhanced fields should not be considered as standard macrosfields but as nonstandard subscale microfields. To illustrate this further, Fig. 14 shows the stress equilibrium equation  $\partial\bar{\sigma}_{22}/\partial x_2 + \partial\bar{\tau}_{12}/\partial x_1$  evaluated along the crack plane,  $x_1 \geq 0$  and  $x_2 = 0$ . The relation should be exactly zero for stationary conditions according to classical theories of continuum mechanics. The microstresses  $\bar{\sigma}_{ij}$  are computed using Hooke's law and the interpolated microstrains  $\bar{\epsilon}_{ij}$  from the union of 100 unique solutions, i.e.  $\bar{\epsilon}_{ij} = [\bar{\sigma}_{ij}(1 + \nu) - \nu\bar{\sigma}_{kk}\delta_{ij}]/E^\mu$ . Thus, the microstresses  $\bar{\sigma}_{ij}$  are always obtained via the microstrains  $\bar{\epsilon}_{ij}$ , interpolated on a regular grid using millions of randomly distributed scattered data points. For the situation of  $\rho = 1$ , i.e. a homogeneous continuum body, the data points are randomly distributed in a similar fashion to the characteristic solutions for porous structures.

As illustrated in Fig. 14, only for the homogeneous continuum ( $\rho = 1$ ), the stress equilibrium is satisfied and the field is divergence-free along  $x_1 \geq 0$ . However, at lower densities the interpolated microstrains  $\bar{\epsilon}_{ij}$  result in microstress fields  $\bar{\sigma}_{ij}$  that are not divergence-free. The physical interpretation of this is definitely not clear. The circumstance that a classical continuum with a scattered LEFM field reproduces  $\partial\bar{\sigma}_{22}/\partial x_2 + \partial\bar{\tau}_{12}/\partial x_1 = 0$  while the averaged solutions capturing 100 unique porous material structures does not is an interesting observation and somehow support the gradient-enhanced theory. Perhaps are subscale microstrains incompatible on a higher scale? Perhaps is the classical continuum equilibrium equation not appropriate for subscale microstresses in materials containing pores, evaluated on a higher scale? These strange peculiarities need to be thoroughly investigated, explained and clearly understood to support, validate and strengthen the gradient-enhanced theory. These essential scientific questions are subjects for future studies. The physics has to be totally understood in order to make this theory trustworthy.

### 5.3. Fracture

It is crucial to establish a physically sound connection between the theoretical gradient sensitivity length  $c$  and any microstructural length in the material. Figs. 11 and 12 reveals that assuming  $c$  is linked to the average pore diameter  $l_c$  seems

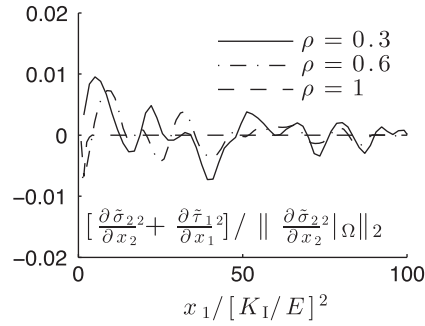


**Fig. 14.** Stress equilibrium equation  $\partial\bar{\sigma}_{22}/\partial x_2 + \partial\bar{\tau}_{12}/\partial x_1$  evaluated along  $x_1 \geq 0$  and  $x_2 = 0$ . The gradients are normalized with the Euclidean norm  $\|\partial\bar{\sigma}_{22}/\partial x_2\|_2$  of all values in the body domain.

to be a fair assumption and allow for direct theoretical estimations of the gradient sensitivity in isotropic porous materials. This finding is also in agreement with an observation in [4] that the fracture mechanism in wood is dominated by the pore size. One may, hence, formulate a crack growth hypothesis as follows: At the pore level, a remote load can produce microcracks. At a crack or defect, these nucleated microcracks most likely appear within a diffuse zone located ahead of a tip and having a size similar to the average pore size. A main crack may eventually coalesce with these microfractures whereupon the crack advances one pore length, i.e. the crack undergoes a step-wise stable growing process. Using  $c = l_c$ , the maximum microstrain in the tip region is estimated to  $\bar{\epsilon}_0 = 0.2\rho K_1/[E l_c^{1/2}]$  and reveal that a larger pore size lower the magnitude of microstrains. This observation is consistent with the findings in e.g. [5] who report that a change to a larger pore size terminates radial crack growth in wood.

Hypothesize that when a maximum subscale microstress  $\bar{\sigma}_{22}$  reaches a certain critical level  $\bar{\sigma}_c$ , cohesive microfracture occur. Assume further that a porous material contain a straight crack of length  $2a \gg l_c$ . Then, according to LEFM, the macroscopic stress intensity factor is given by  $K_1 = \sigma_0[2\pi a]^{1/2}$  where  $\sigma_0$  is a remote uniaxial global stress acting far away from the crack. Applying the micro/macro stiffness approximation in (1), using  $c = l_c$  and  $\nu = 0.3$ , the relation (10) gives that  $\max\{\bar{\sigma}_{22}\} \approx 0.3K_1/[\rho l_c^{1/2}]$ . Since  $K_1 = \sigma_0[2\pi a]^{1/2}$  a subscale cohesive microstress in transversely isotropic porous materials can be estimated to:

$$\bar{\sigma}_c \approx 0.75 \frac{\sigma_0}{\rho} \left[ \frac{a}{l_c} \right]^{1/2}. \tag{13}$$

Eq. (13) link the cohesive subscale microstress  $\bar{\sigma}_c$  to the remote macroscopic stress  $\sigma_0$ . It would thus be possible to estimate  $\bar{\sigma}_c$  in standard laboratory fracture tests.

5.4. Note on interpolation

The interpolated strains  $\bar{\epsilon}_{22}$  are dependent on the grid density in the interpolation procedure. A too dense grid produce scattered results, because too few data points are available in each cell, while a too sparse grid become too low-resolved and produce too averaged and smoothened values. It is, thus, a tricky balance act finding optimum settings. Using the grid resolution described in Section 4, in combination with a typical number of scattered data points, the applied interpolation and

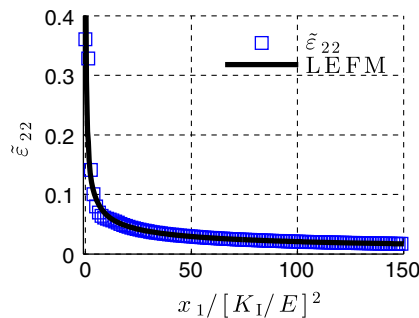


**Fig. 15.** Microstrains  $\bar{\epsilon}_{22}$  at  $\rho = 1$  (i.e.  $l_c = 0$ ) interpolated on a grid from randomly distributed and scattered data points of a pure LEFM field. Also shown is the theoretical LEFM singular strain.

smoothing procedure is able to capture a randomly distributed classical singular LEFM field well, Fig. 15, which lend some confidence in the chosen grid density.

## 6. Conclusions

The gradient-enhanced theory seems to offer a fairly good approximation of near-tip subscale microstrain fields in porous isotropic materials. To judge the theory's ability to capture mechanical behavior in porous materials, subscale microstrain fields  $\bar{\varepsilon}_{22}$  in the near-tip regions of stationary mode I cracks, given by the model, are contrasted with microstrain fields  $\tilde{\varepsilon}_{22}$  computed from high-resolution finite element microstructural models of randomly distributed pores with different pore sizes and densities but similar macroscopic geometry and boundary conditions. When comparing the results in Figs. 10–13 one sees that the two microstrain fields,  $\bar{\varepsilon}_{22}$  and  $\tilde{\varepsilon}_{22}$ , are surprisingly similar. The relatively simple gradient-enhanced continuum theory produces remarkably similar subscale microscopic fields as the considerably more computationally demanding discrete microstructural models and seems to be able to approximate subscale length-effects in a convenient and general way, despite the physical peculiarity of divergence and incompatibility of the gradient-enhanced subscale fields discussed in connection to (10) and Section 5.2. However, these issues need to be thoroughly investigated, explained and clearly understood to support, validate and strengthen the gradient-enhanced theory. The theory thus needs further investigations and deeper physical understanding to be convincing, trustworthy and reliable. Nevertheless, a key observation in this study is that the internal characteristic length parameter, used in the gradient-enhanced model, seems to be linked to the average pore diameter, allowing for theoretical bridging between scales. A relatively larger pore size results in a relatively lower magnitude of the subscale microstrain field in the tip region (11). Finally, the gradient-enhanced theory seems to be consistent with an experimentally observed tendency in radial fracture in wood. However, limitations in resolution and the image correlation analysis, and difficulties to localize the physical crack tip, make it very hard to draw trustworthy and convincing conclusions from the experiment. We also need more experiments to obtain statistically reliable observations. Some trends may be imagined that seem to indicate that the position of maximum strain is ahead of the tip at a distance that appears to correspond roughly to some average pore diameter. However, we need to obtain higher resolved CT images to be sure and to be able to draw stronger conclusions.

## Acknowledgements

The authors are thankful for the financial support from the Swedish Research Council Formas (grant no. 232-2014-202).

## References

- [1] Smith I. *Fracture and fatigue in wood*. John Wiley & Sons; 2003.
- [2] Vasic S, Smith I, Landis E. Finite element techniques and models for wood fracture mechanics. *Wood Sci Technol* 2005;39:3–17.
- [3] Hägglund R, Isaksson P. Influence of damage in the vicinity of a macrocrack tip in embossed paper. *Eng Fract Mech* 2007;74:1758–69.
- [4] Thuvander F, Berglund LA. In situ observations of fracture mechanisms for radial cracks in wood. *J Mater Sci* 2000;35:6277–83.
- [5] Stanzl-Tschegg SE, Keunecke D, Tschegg EK. Fracture tolerance of reaction wood (yew and spruce wood in the TR crack propagation system). *J Mech Behav Biomed Mater* 2011;4:688–98.
- [6] Barenblatt GI. The mathematical theory of equilibrium cracks in brittle fracture. *Adv Appl Mech* 1962;7:55–129.
- [7] Dugdale DS. Yielding of steel sheets containing slits. *J Mech Phys Solids* 1960;8:100–4.
- [8] Toupin R. Elastic materials with couple-stresses. *Arch Rat Mech Anal* 1962;11:385–414.
- [9] Kröner E. On the physical reality of torque stresses in continuum mechanics. *Int J Eng Sci* 1963;1:261–78.
- [10] Mindlin R. Micro-structure in linear elasticity. *Arch Rat Mech Anal* 1964;16:52–78.
- [11] Kröner E. Elasticity theory of materials with long range cohesive forces. *Int J Solids Struct* 1967;3:731–42.
- [12] Eringen AC, Edelen DGB. On nonlocal elasticity. *Int J Eng Sci* 1972;10:233–48.
- [13] Eringen AC. On differential equations of nonlocal elasticity and solutions of screw dislocation and surface waves. *J Appl Phys* 1983;54:4703–10.
- [14] Triantafyllidis N, Aifantis EC. A gradient approach to localization of deformation. I. Hyperelastic materials. *J Elast* 1986;16:225–37.
- [15] Aifantis EC. Update on a class of gradient theories. *Mech Mater* 2003;35:259–80.
- [16] Aifantis EC. On the gradient approach – relation to Eringen's nonlocal theory. *Int J Eng Sci* 2011;49:1367–77.
- [17] Askes H, Aifantis EC. Gradient elasticity in statics and dynamics: an overview of formulations, length scale identification procedures, finite element implementations and new results. *Int J Solids Struct* 2011;48:1962–90.
- [18] Aifantis EC. Gradient material mechanics: perspectives and prospects. *Acta Mech* 2014;225:999–1012.
- [19] Isaksson P, Hägglund R. Structural effects on deformation and fracture of random fiber networks and consequences on continuum models. *Int J Solids Struct* 2009;46:2320–9.
- [20] Isaksson P, Hägglund R. Crack-tip fields in gradient-enhanced elasticity. *Eng Fract Mech* 2013;97:186–92.
- [21] Isaksson P, Dumont PJJ. Approximation of mode I crack-tip displacement fields by a gradient-enhanced elasticity theory. *Eng Fract Mech* 2014;117:1–11.
- [22] Fleck NA, Muller GM, Ashby MF, Hutchinson JW. Strain gradient plasticity: theory and experiment. *Acta Metall Mater* 1994;42:475–87.
- [23] Fleck NA, Hutchinson JW. A reformulation of strain gradient plasticity. *J Mech Phys Solids* 2001;49:2245–71.
- [24] Gurtin ME, Anand L. Thermodynamics applied to gradient theories involving the accumulated plastic strain: the theories of Aifantis and Fleck and Hutchinson and their generalization. *J Mech Phys Solids* 2009;57:405–21.
- [25] Jernkvist LO. On the fracture behaviour of softwood: a combined experimental and computational study of the interaction between fracture behaviour and material anatomy PhD Thesis. Luleå Univ. of Tech.; 2000.
- [26] Blaber J, Adair B, Antoniou A. Ncorr: open-source 2D digital image correlation matlab software. *Exp Mech* 2015;55:1105–22.
- [27] Gibson LJ, Ashby MF. *Cellular solids: structure and properties*. Cambridge University Press; 1999.
- [28] Williams ML. On the stress distribution at the base of a stationary crack. *J Appl Mech* 1957;24:109–14.
- [29] Altan BS, Aifantis EC. On some aspects in the special theory of gradient elasticity. *J Mech Behav Mater* 1997;8:231–82.
- [30] Lasry D, Belytschko T. Localization limiters in transient problems. *Int J Solids Struct* 1988;24:581–97.

- [31] Aifantis EC. A note on gradient elasticity and nonsingular crack fields. *J Mech Behav Mater* 2011;20:103–5.
- [32] Gurtin ME, Anand L. A theory of strain-gradient plasticity for isotropic, plastically irrotational materials. Part I: Small deformations. *J Mech Phys Solids* 2005;53:1624–49.
- [33] Askes H, Gitman A. Review and critique of the stress gradient elasticity theories of Eringen and Aifantis. In: Maugin GA, Metrikine AV, editors. *Mechanics of Generalized Continua. Advances in Mechanics and Mathematics*. New York: Springer; 2010.
- [34] Ru CQ, Aifantis EC. A simple approach to solve boundary-value problems in gradient elasticity. *Acta Mech* 1993;101:59–68.
- [35] Matlab. Version 2015a. The MathWorks Inc., Natick, MA.
- [36] Persson PO, Strang G. A simple mesh generator in MATLAB. *SIAM Rev* 2004;46:329–45.
- [37] Garcia D. Robust smoothing of gridded data in one and higher dimensions with missing values. *Comput Stat Data Anal* 2010;54:1167–78.
- [38] Garcia D. A fast all-in-one method for automated post-processing of PIV data. *Exp Fluids* 2011;50:1247–59.
- [39] Aifantis EC. On non-singular GRADELA crack-fields. *Theor Appl Mech Lett* 2014;4:051005.
- [40] Hutchinson JW. Generalizing  $J_2$  flow theory: fundamental issues in strain gradient plasticity. *Acta Mech Sinica* 2012;28:1078–86.
- [41] Gudmundson P. A unified treatment of strain gradient plasticity. *J Mech Phys Solids* 2004;52:1379–406.
- [42] Fleck NA, Hutchinson JW. Strain gradient plasticity. *Adv Appl Mech* 1997;33:295–361.
- [43] Aifantis EC. The physics of plastic deformation. *Int J Plast* 1987;3:211–47.
- [44] Huang Y, Gao H, Nix WD, Hutchinson JW. Mechanism-based strain gradient plasticity – II. Analysis. *J Mech Phys Solids* 2000;48:99–128.
- [45] Gitman IM, Askes H, Kuhl E, Aifantis EC. Stress concentrations in fractured compact bone simulated with a special class of anisotropic gradient elasticity. *Int J Solids Struct* 2010;47:1099–107.
- [46] Isaksson P. A note on stress fields and crack growth in porous materials subjected to a contact load. *Int J Solids Struct* 2015;64:62–70.
- [47] Askes H, Susmel L. Understanding cracked materials: is Linear Elastic Fracture Mechanics obsolete? *Fatigue Fract Eng Mater Struct* 2015;38:154–60.